AGU PUBLICATIONS

Global Biogeochemical Cycles

RESEARCH ARTICLE
10.1002/2016GB005600

Key Points:
- We provide probabilistic estimates of trends, and their errors, in satellite derived ocean chlorophyll using Bayesian space-time modeling
- We show that including spatial correlation in a statistical model improves fit accuracy and provides a more complete uncertainty assessment
- We show that the global trend in ocean chlorophyll from a space-time model is reduced with implications for studying global long-term change

Supporting Information:
- Supporting Information S1

Correspondence to:
M. L. Hammond,
matthew.hammond@soton.ac.uk

Citation:
Hammond, M. L., C. Beaulieu, S. K. Sahu, and S. A. Henson (2017), Assessing trends and uncertainties in satellite-era ocean chlorophyll using space-time modeling, *Global Biogeochem. Cycles*, *31*, doi:10.1002/2016GB005600.

Received 8 DEC 2016
Accepted 14 JUN 2017
Accepted article online 15 JUN 2017

Assessing trends and uncertainties in satellite-era ocean chlorophyll using space-time modeling

Matthew L. Hammond[1], Claudie Beaulieu[1], Sujit K. Sahu[2], and Stephanie A. Henson[3]

[1]Ocean and Earth Science, University of Southampton, Southampton, UK, [2]Mathematical Sciences, University of Southampton, Southampton, UK, [3]National Oceanography Centre, Southampton, UK

Abstract The presence, magnitude, and even direction of long-term trends in phytoplankton abundance over the past few decades are still debated in the literature, primarily due to differences in the data sets and methodologies used. Recent work has suggested that the satellite chlorophyll record is not yet long enough to distinguish climate change trends from natural variability, despite the high density of coverage in both space and time. Previous work has typically focused on using linear models to determine the presence of trends, where each grid cell is considered independently from its neighbors. However, trends can be more thoroughly evaluated using a spatially resolved approach. Here a Bayesian hierarchical spatiotemporal model is fitted to quantify trends in ocean chlorophyll from September 1997 to December 2013. The approach used in this study explicitly accounts for the dependence between neighboring grid cells, which allows us to estimate trend by "borrowing strength" from the spatial correlation. By way of comparison, a model without spatial correlation is also fitted. This results in a notable loss of accuracy in model fit. Additionally, we find an order of magnitude smaller global trend, and larger uncertainty, when using the spatiotemporal model: $-0.023 \pm 0.12\%\ yr^{-1}$ as opposed to $-0.38 \pm 0.045\%\ yr^{-1}$ when the spatial correlation is not taken into account. The improvement in accuracy of trend estimates and the more complete account of their uncertainty emphasize the solution that space-time modeling offers for studying global long-term change.

1. Introduction

Phytoplankton produces approximately half of the global total primary production (PP), forming the foundation of all marine ecosystems [*Field et al*., 1998]. Quantifying how phytoplankton abundance may be affected by climate change is the key to predicting the magnitude and direction of future changes in fisheries and marine ecosystems [*Hoegh-Guldberg et al*., 2014]. The distribution of phytoplankton is primarily controlled by the degree of stratification which, in turn, affects nutrient supply and light exposure [*Doney*, 2006]. Global warming has the potential to increase stratification, affecting phytoplankton distribution and abundance. A useful proxy for stratification is sea surface temperature (SST), which is predicted to increase over both the near and long terms [e.g., *Collins et al*., 2013; *Kirtman et al*., 2013]. Climate change is also predicted to affect wind and ocean circulation patterns, and decrease sea ice volumes [e.g., *England et al*., 2014; *Moore et al*., 2015], with uncertain effects on phytoplankton.

To date, the most comprehensive information on phytoplankton abundance and distribution comes from the proxy chlorophyll *a* (chl) measured by ocean color satellites at a high spatial and temporal resolution. Previous attempts to determine the presence of trends in ocean color data have produced a wide range of results. For example, a global average positive trend was reported by *Antoine et al*. [2005], using data from both the Coastal Zone Color Scanner (1979–1986) and the first 4 years of the Sea-Viewing Wide Field-of-View Sensor (SeaWiFS) data (1998–2002). Using solely SeaWiFS data, *Behrenfeld et al*. [2006] (over the period 1997–2006) and *Vantrepotte and Mélin* [2011] (over the period 1997–2007) found that PP and chl show a decrease over much of the global ocean. Studies that consider temporal autocorrelation in their statistical analyses show either a low magnitude positive trend or that no global trend can yet be distinguished from noise. For example, a low magnitude global positive trend was reported by *Saulquin et al*. [2013] combining data from SeaWiFS (September 1997 to December 2010) and the Medium Resolution Imaging Spectrometer (MERIS) (April 2002 to April 2012) instruments. In another analysis, using solely SeaWiFS data (September 1997 to December 2008), *Beaulieu et al*. [2013] show that no global trend can be distinguished from noise, for which a time series of approximately 40 years length would be required [*Henson et al*., 2010]. This length could represent a minimum as the presence of discontinuities in the record may increase the number of years required to detect a given trend [*Beaulieu et al*., 2013].

In a compilation of historical, in situ, ocean transparency data *Boyce et al*. [2010] showed a decline of approximately 1% yr^{-1} over the past 100 years. There have been criticisms of the methodology used, due to the lack of uniformity in collection techniques and the large rate of decrease reported [e.g., *Rykaczewski and Dunne*, 2011; *Siegel et al*., 2013]. However, these criticisms were addressed in a subsequent work, which produced very similar findings [*Boyce et al*., 2014].

The major challenges affecting trend detection in chl include the low signal-to-noise ratio, observational gaps, and the large degree of natural variability inherent in the system [e.g., *Saulquin et al*., 2013]. In addition, the use of simple linear temporal models in recent studies does not effectively use all the information provided by observations, ignoring the effects of spatial correlation. Including this feature in the model offers the potential to improve detection power by borrowing strength from neighboring observations [*Chandler and Scott*, 2011]. More generally, a spatially resolved model would better reflect the physical reality, where chl evolves in a spatially and temporally correlated fashion, and improve long-term trend estimates and their uncertainty. Therefore, this study focuses on assessing the probabilities of long-term trends in ocean chl using (a) the longer time series provided by the ESA OC-CCI (the Ocean Color project in the European Space Agency's Climate Change Initiative) data and (b) a Bayesian hierarchical spatiotemporal approach allowing spatial correlation to be considered. By using the Bayesian spatiotemporal model we expect to improve the accuracy of chl trend estimates and provide a more complete account of their uncertainty.

2. Materials and Methods

2.1. Data

The chl data come from version 2.0 of ESA's OC-CCI project ([*Lavender et al*., 2015], available at http://www.esa-oceancolour-cci.org/). This combines data from the SeaWiFS, MERIS, and the Moderate Resolution Imaging Spectroradiometer sensors in order to create a continuous, bias-corrected time series running from September 1997 to December 2013 inclusive. The resulting time series is approximately 50% longer than the longest individual data set (SeaWiFS, after removal of post-2007 data due to telemetry issues). The ESA project uses band-shifting and bias-correction techniques to combine data from the individual sensors. For this study we downscale the resultant data set from a 1/24° grid to a 1° grid by averaging within 1° boxes. The chl values are then lognormal transformed after *Campbell* [1995]. To help explain the natural variability in the chl data, SST is included as a covariate. SST data are sourced from the NOAA optimum interpolation v2 data product ([*Reynolds et al*., 2002], available at http://www.esrl.noaa.gov/psd/data/gridded/data.noaa.oisst.v2.html). Monthly means are used in both data sets.

The data are divided into 54 regions, as defined by *Longhurst* [1995, 1998], according to characteristic physical forcing and biogeochemical factors. Coastal and polar waters are excluded from this analysis due to issues with data availability and quality. Coastal regions are omitted from the analysis due to higher uncertainties in ocean color data arising from constituents in the water column and issues removing contamination from atmospheric dust and sulfates from continental sources. Polar regions are excluded due to the high proportion of missing data, primarily due to cloud cover, which can cover 90% of the sky during ice-free periods and has increased over recent years [*Bélanger et al*., 2013]. Both these effects vary independently of chl and are thus challenging to compensate for [*Schollaert et al*., 2003; *Hyde et al*., 2007; *Mélin et al*., 2007]. Coastal and polar regions are defined as in *Longhurst* [1998]. This leaves 23 regions in which the analysis is performed.

2.2. Model Formulation

A hierarchical Bayesian spatiotemporal model is fitted separately to chl data in each of the 23 Longhurst regions used in this analysis. The key equations are presented below (see Table 1 for a list of all parameter definitions), and a representative diagram is included in Figure 1. In the first level, the model describes the relationship between the true and the observed chl:

$$Z_{n,t} = O_{n,t} + \varepsilon_{n,t} \tag{1}$$

where $Z_{n,t}$ is the observed chl at location n and at month t. This is composed of the corresponding true chl value $O_{n,t}$ and a white noise process $\varepsilon_{n,t}$ which arises primarily due to random measurement error. This error is assumed independently normally distributed with a zero mean and unknown pure error variance: σ_ε^2, i.e., $\varepsilon_{1,t}, \ldots, \varepsilon_{N,t} \sim \left(N\left(\mathbf{0}, \sigma_\varepsilon^2 \boldsymbol{I}_n\right)\right)$ for all t. The true chl value is represented by the following regression model:

Table 1. Definition of Parameters Used in the Equations

Character	Definition
$\boldsymbol{a}_n^{'}$	Kriging coefficients between the random effects at the observation and knot locations
$\boldsymbol{C}_n^{'}$	Cross-correlation vector of the spatial random effects
$\boldsymbol{I}_n$	Identity matrix of order n
K_v	Modified Bessel function
M	Total number of knot locations
m	Knot locations
N	Total number of observation locations
n	Observation locations
O	True chl values
$\boldsymbol{S}_w$	Spatial correlation matrix of the reduced set of spatiotemporal random effects
$\boldsymbol{S}_0$	Initial spatial correlation matrix
T	Total duration of time series (months)
t	Time (months)
$\boldsymbol{w}$	Reduced set of spatiotemporal random effects at knot locations
$\boldsymbol{x}$	Design matrix
Z	Observed chl values
$\overline{Z}$	Regional mean of observed chl values
$\boldsymbol{\beta}$	Parameters (intercept and covariates)
$\boldsymbol{\gamma}$	m dimensional Gaussian process
ε	Random pure error
$\boldsymbol{\eta}$	Spatiotemporal random effects at observation locations
$\boldsymbol{\theta}$	The parameters: $\boldsymbol{\beta}$, ρ, σ_0^2, σ_ε^2, σ_w^2, Φ, ν
v	Smoothness of the random field in spatial correlation
ρ	Unspecified autoregressive term
σ_0^2	Initial variance condition
σ_ε^2	Unknown pure error variance
σ_w^2	Site invariant spatial variance
Φ	Spatial correlation parameter

$$O_{n,t} = \boldsymbol{x}'_{n,t}\boldsymbol{\beta} + \boldsymbol{a}_n^{'}\boldsymbol{w}_t \tag{2}$$

composed of the covariates (including intercept) $\boldsymbol{x}_{n,t}$, the regression coefficients $\boldsymbol{\beta}$, and the term $\boldsymbol{a}_n^{'}\boldsymbol{w}_t$ representing spatial and temporal correlation, the second level, defined in detail below. The covariates include time, month (represented as factor levels whereby each month of the year has its own additional term, i.e., a value constant for all years, is added or subtracted for each month), and SST. Time is used to estimate the temporal trend, the monthly factor to isolate the seasonal cycle, and SST is included due to its strong influence on chl variability.

In the second level, a Gaussian Predictive Process-type model is used to calculate the spatiotemporal random effects. This process is used to improve computational speed for the large sets of spatiotemporal data in this study [*Banerjee et al*., 2008; *Finley et al*., 2009; *Sahu and Bakar*, 2012]. This model type calculates the spatiotemporal process (random effects) $\boldsymbol{\eta}_t$ at the knot sites, a subset $\boldsymbol{m}$ of the observation locations $\boldsymbol{n}$, providing the reduced set of random effects $\boldsymbol{w}_t$. The Gaussian Predictive Process reduces computational time by decreasing the size of the spatial covariance matrix, which must be inverted at each iteration of the Gibbs sampling Markov Chain Monte Carlo algorithm. Kriging is then used to expand the reduced spatial covariance matrix to the complete set of observation locations after the inversion at each iteration. The spatiotemporal random effects between the knot and observation locations are given by $\boldsymbol{a}_n^{'}\boldsymbol{w}_t$ where $\boldsymbol{a}_n^{'}$ is

$$\boldsymbol{a}_n^{'} = \boldsymbol{C}_n^{'}\boldsymbol{S}_w^{-1} \tag{3}$$

where $\boldsymbol{C}_n^{'}$ is the correlation vector of the spatial random effects between the $\boldsymbol{n}$ observation locations and the $\boldsymbol{m}$ knot locations, and $\boldsymbol{S}_w$ is the correlation matrix of the reduced set of random effects ($\boldsymbol{w}_t$).

The correlation matrix $\boldsymbol{S}_w$ is obtained using the Matérn correlation function [*Handcock and Stein*, 1993; *Handcock and Wallis*, 1994]:

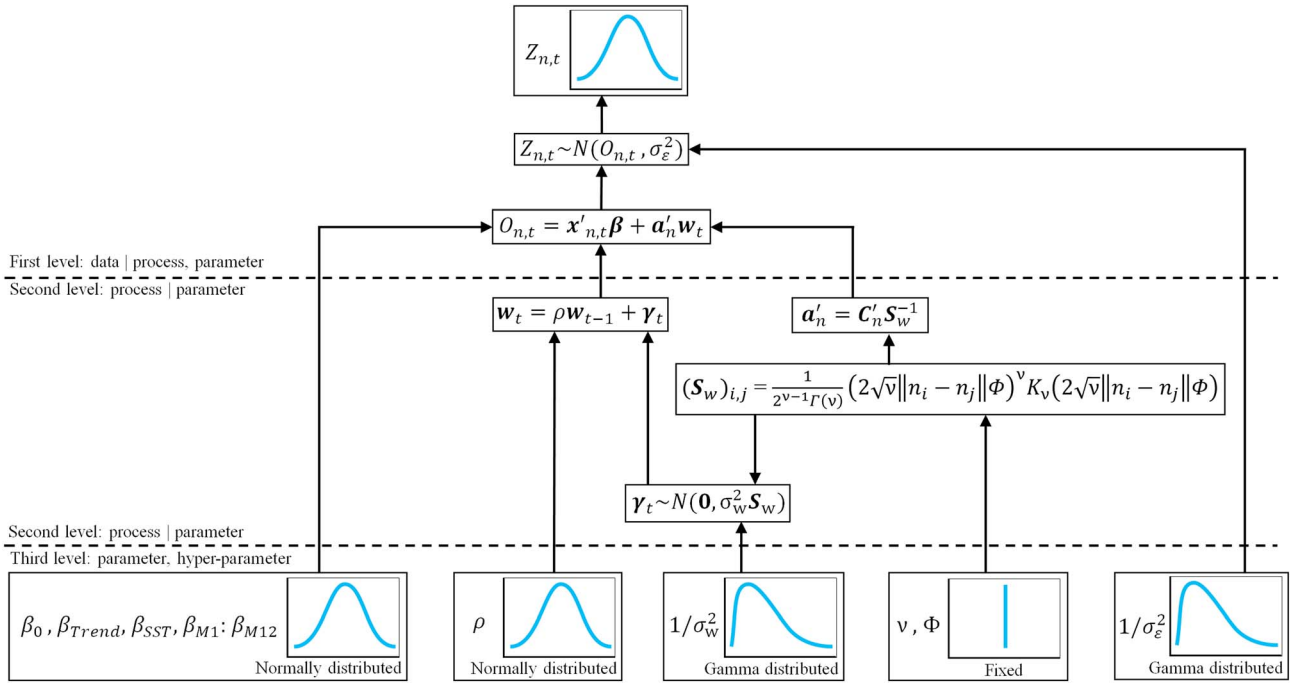

Figure 1. Flowchart describing the three levels of the model and linkages among the processes, parameters, and hyper-parameters. At the first level, the model describes the process generating the chl data, in which the chl observations are represented by a linear regression model, white noise, and a spatiotemporal process. At the second level, the spatiotemporal process is calculated based on the parameters. At the third level, the prior distributions of the parameters are described with the use of hyper-parameters. See section 2.2 and Table 1 for definition of model parameters.

$$\kappa(n_i, n_j; \Phi, \nu) = \frac{1}{2^{\nu-1}\Gamma(\nu)} \left(2\sqrt{\nu}\|n_i - n_j\|\Phi\right)^{\nu} K_\nu \left(2\sqrt{\nu}\|n_i - n_j\|\Phi\right), \quad \Phi > 0, \nu > 0 \tag{4}$$

where $\Gamma(\nu)$ is the standard gamma function, K_ν is the modified Bessel function (second kind) with order ν, and $\|n_i - n_j\|$ is the distance between two sites n_i and n_j. The decay parameter Φ controls how the correlation decays as the distance between the two sites becomes larger and is assigned a value based on testing (see supporting information). The parameter ν represents smoothness of the random field and is assigned a value of 0.5, representing an exponential covariance function.

The random effects, specified at the m knot sites, are expressed as

$$\boldsymbol{w}_t = \rho \boldsymbol{w}_{t-1} + \boldsymbol{\gamma}_t \tag{5}$$

where $\boldsymbol{w}_{t-1}$ are the random effects at the month immediately prior to t, ρ is an unknown autoregressive term assumed to be in the interval $(-1,1)$, and $\boldsymbol{\gamma}_t$ is the M dimensional Gaussian process: $N(\boldsymbol{0}, \boldsymbol{\Sigma}_w)$, where $\boldsymbol{\Sigma}_w = \sigma_w^2 \boldsymbol{S}_w$ (σ_w^2 is the site invariant spatial variance). The autoregressive model (equation (5)) is completed by assuming the initial condition: $\boldsymbol{w}_0 \sim N(0, \sigma_0^2 S_0)$.

The third level of the model represents the prior distributions of the parameters used in the first two levels. Flat priors are used to reflect the lack of prior knowledge about the trend value and other parameters of the model. Additional details on the prior and posterior distributions are presented in the discussion and supporting information.

This approach provides a full posterior distribution for each parameter fitted in the model. Here we focus on the trend parameter whose best estimate corresponds to the posterior mode and whose uncertainty is represented by a 95% credible interval, which is defined as the 95% highest posterior density interval [*Kruschke*, 2015]. As a decision rule, we consider that if the 95% credible interval contains the value 0 it is unlikely that a trend is present. The number of regions exhibiting trends thus depends on this decision rule.

To assess the benefit of including spatial correlation in the model, two models are fitted using different values of Φ: the first model uses the value of Φ determined as optimal by fitting, while the second model uses a

value of $\Phi = 1000$ which effectively removes spatial correlation (see supporting information). The two fits are compared using the normalized root-mean-square error (NRMSE) for each region:

$$NRMSE = \frac{\sqrt{\frac{\sum_{n=1}^{N}\sum_{t=1}^{T}\left(O_{n,t}-Z_{n,t}\right)^2}{NT}}}{\overline{Z}} \quad (6)$$

where NT represents the total number of data points in each region and $\overline{Z}$ the mean observed chl concentration within a region. A NRMSE of zero indicates a perfect fit. Large NRMSE values indicate misfit, but do not reveal whether the model overestimates or underestimates the observations. Thus, bias is used to provide this information. Again, a bias of zero indicates a perfect fit.

$$\text{Bias} = \sum_{n=1}^{N}\sum_{t=1}^{T}\left(O_{n,t} - Z_{n,t}\right) \quad (7)$$

The model fit is obtained using the spTimer package in R [*Bakar and Sahu*, 2015]. For full details on the methodology, the reader should refer to *Bakar and Sahu* [2015].

3. Results

3.1. Model Accuracy and Trend Uncertainty

We compare the model fit, and uncertainties in our trend estimates, between the model with spatial correlation and the model without spatial correlation in each individual region (Figure 2 and Table 2). The NRMSE and bias are systematically reduced in all regions when using the spatiotemporal model, showing notable improvement in accuracy. For some regions such as the North Atlantic Tropical Gyral Province (Region 4) and the South Pacific Subtropical Gyre Province (Region 20), the NRMSE and bias are improved by at least 200% in the spatiotemporal model when compared to the model without spatial correlation. In addition, the uncertainties in the trend magnitude are all larger in the spatiotemporal model without exception.

Figure 2 shows the larger uncertainty in the spatiotemporal model for all regions except the Subantarctic Province (Region 22). In the spatiotemporal model, the widest 95% credible intervals (i.e., highest uncertainty) are found in the Kuroshio Current Province (Region 12) and the North Atlantic Subtropical Gyral Province (East) (Region 14). The narrowest 95% credible intervals (i.e., most robust trends) are found in the Southern Ocean, i.e., the South Subtropical Convergence Province (Region 21) and the Subantarctic Province (Region 22). There does not seem to be any relationship between the size of the 95% credible intervals and the magnitude/sign of change.

In both cases, the global trend and uncertainty are estimated by weighting each region's upper and lower 95% credible interval boundaries, and mode posterior trend, by their area and average chlorophyll concentration, relative to a global total of these values. The global uncertainty is 3 times larger in the model with spatial correlation, i.e., the 95% credible interval width is 0.12% yr^{-1} in the model with spatial correlation and 0.045% yr^{-1} in the model without spatial correlation. Note that this excludes polar and coastal regions for which the model is not run.

3.2. Trend Differences

The trend magnitudes for each region obtained by the spatiotemporal model and the model without spatial correlation are presented in Table 2 and Figures 2 and 3. In the spatiotemporal model there is no consistent direction of trend among the regions. Instead, the oceans are divided between areas of general increase and decrease. The spatiotemporal model shows no global change: $-0.023 \pm 0.12\%\ yr^{-1}$, as opposed to a total global decline of $0.38 \pm 0.045\%\ yr^{-1}$ in the model without spatial correlation, where a greater number of regions show a decline. The most noticeable differences are in the northern high-latitude regions and the North Pacific where positive trends are detected when including spatial correlation, as opposed to negative trends when spatial correlation is not included.

In the model with spatial correlation (Figure 3a), the highest latitude regions all show a positive trend. It is also notable that positive trends are both more frequent and higher in magnitude in the Northern Hemisphere. The strongest positive trends both lie on the eastern boundaries of basins: $0.72 \pm 0.20\%\ yr^{-1}$ in the North Pacific Tropical Gyre Province (Region 6) and $0.97 \pm 0.28\%\ yr^{-1}$ in the North Atlantic Subtropical Gyral

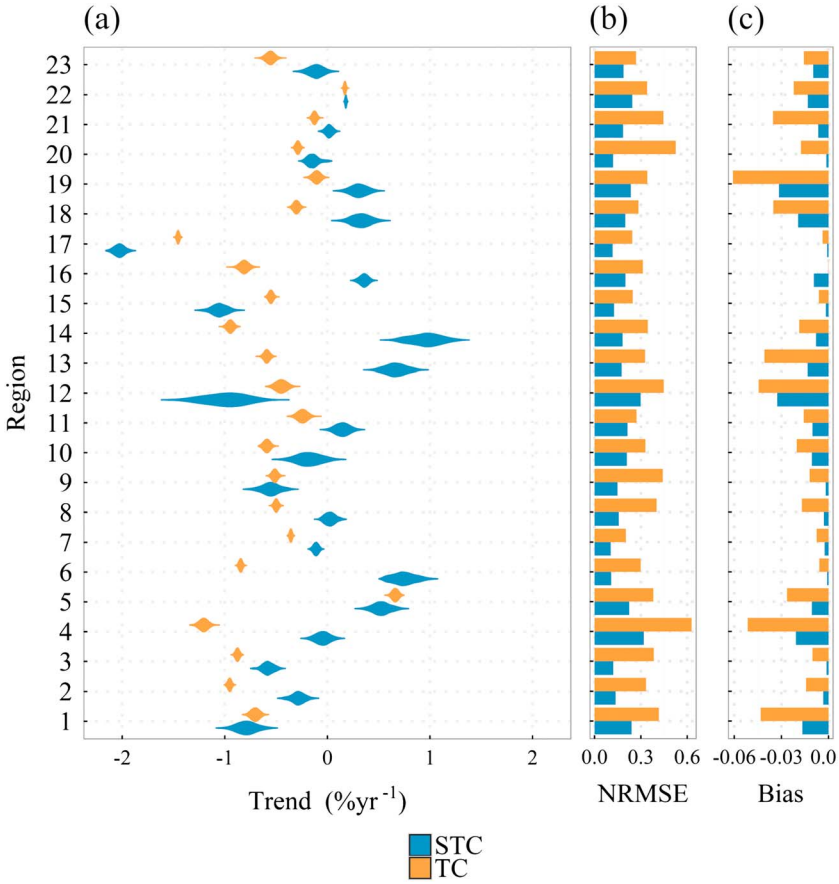

Figure 2. (a) Posterior probability densities for the chl trends obtained in each region, (b) accuracy of the fit via the normalized root-mean-square error (NRMSE) for each region, and (c) the general direction of any misfit (bias). Two models are used in each region: STC refers to the model with spatiotemporal correlation and TC refers to the model with temporal correlation only (i.e., without spatial correlation). The regions are as follows: (1) Eastern Tropical Atlantic Province, (2) Indian Monsoon Gyres Province, (3) Indian South Subtropical Gyre Province, (4) North Atlantic Tropical Gyral Province, (5) North Pacific Equatorial Countercurrent Province, (6) North Pacific Tropical Gyre Province, (7) Pacific Equatorial Divergence Province, (8) South Atlantic Gyral Province, (9) West Pacific Warm Pool Province, (10) Western Tropical Atlantic Province, (11) Gulf Stream Province, (12) Kuroshio Current Province, (13) North Atlantic Drift Province, (14) North Atlantic Subtropical Gyral Province (East), (15) North Atlantic Subtropical Gyral Province (West), (16) North Pacific Polar Front Province, (17) North Pacific Subtropical Gyre Province (West), (18) Pacific Subarctic Gyres Province (East), (19) Pacific Subarctic Gyres Province (West), (20) South Pacific Subtropical Gyre Province, (21) South Subtropical Convergence Province, (22) Subantarctic Province, and (23) Tasman Sea Province.

Province (East) (Region 14). The strongest negative trends can be seen in the Northern Hemisphere western subtropical gyral provinces, with trends of $-1.1 \pm 0.16\%$ yr^{-1} in the North Atlantic (Region 15) and $-2.0 \pm 0.10\%$ yr^{-1} in the North Pacific (Region 17). Most provinces in the Equatorial and Southern Atlantic, specifically the North Atlantic Tropical Gyral Province (Region 4), the South Atlantic Gyral Province (Region 8), and the Western Tropical Atlantic Province (Region 10), do not exhibit a trend (95% credible interval). The South Pacific subtropical Gyre Province (Region 20), the South Subtropical Convergence Province (Region 21), and the Tasman Sea Province (Region 23) also do not exhibit a trend (95% credible interval).

In the model without spatial correlation (Figure 3b), 21 of the 23 regions show a negative trend, and the two regions with positive trends are the North Pacific Equatorial Countercurrent Province (Region 5) ($0.67 \pm 0.06\%$ yr^{-1}) and the Subantarctic Province (Region 22) ($0.17 \pm 0.02\%$ yr^{-1}). By contrast with the model that considers spatial correlation, every region is deemed likely to have a trend. The negative trends range from $-1.5 \pm 0.03\%$ yr^{-1} in the North Pacific Subtropical Gyre Province (West) (Region 17) to $-0.10 \pm 0.07\%$ yr^{-1} in the Pacific Subarctic Gyres Province (West) (Region 19). Although there is a considerable amount of variability in the magnitude of trends between regions there does not seem to be any discernible pattern relating to latitude.

Table 2. Summary of Trend Estimates for All Regions, Their 95% Credible Interval Representing the Uncertainty, and Model Goodness of Fit, Measured by the Normalized-Root-Mean-Square Error (NRMSE) and Bias[a]

Region	Model Type	Trend Value	Lower CI	Upper CI	NRMSE	Bias
1	STC	**−0.79**	**−0.97**	**−0.58**	**0.24**	**−0.02**
	TC	**−0.70**	**−0.78**	**−0.63**	**0.42**	**−0.04**
2	STC	**−0.29**	**−0.43**	**−0.16**	**0.14**	**0.00**
	TC	**−0.95**	**−0.99**	**−0.92**	**0.33**	**−0.01**
3	STC	**−0.58**	**−0.68**	**−0.46**	**0.12**	**0.00**
	TC	**−0.87**	**−0.91**	**−0.84**	**0.38**	**−0.01**
4	STC	−0.029	−0.19	0.093	0.32	−0.02
	TC	**−1.21**	**−1.29**	**−1.13**	**0.63**	**−0.05**
5	STC	**0.54**	**0.36**	**0.70**	**0.23**	**−0.01**
	TC	**0.67**	**0.60**	**0.72**	**0.38**	**−0.03**
6	STC	**0.72**	**0.55**	**0.95**	**0.11**	**0.00**
	TC	**−0.84**	**−0.88**	**−0.81**	**0.30**	**−0.01**
7	STC	**−0.11**	**−0.16**	**−0.06**	**0.10**	**0.00**
	TC	**−0.35**	**−0.38**	**−0.33**	**0.20**	**−0.01**
8	STC	0.034	−0.068	0.13	0.16	0.00
	TC	**−0.50**	**−0.54**	**−0.46**	**0.40**	**−0.02**
9	STC	**−0.57**	**−0.73**	**−0.37**	**0.15**	**0.00**
	TC	**−0.51**	**−0.57**	**−0.46**	**0.44**	**−0.01**
10	STC	−0.21	−0.42	0.05	0.24	−0.01
	TC	**−0.58**	**−0.65**	**−0.53**	**0.33**	**−0.02**
11	STC	**0.16**	**0.01**	**0.29**	**0.21**	**−0.01**
	TC	**−0.24**	**−0.33**	**−0.16**	**0.27**	**−0.02**
12	STC	**−0.93**	**−1.41**	**−0.62**	**0.30**	**−0.03**
	TC	**−0.44**	**−0.55**	**−0.35**	**0.45**	**−0.04**
13	STC	**0.64**	**0.47**	**0.87**	**0.18**	**−0.01**
	TC	**−0.59**	**−0.64**	**−0.54**	**0.33**	**−0.04**
14	STC	**0.97**	**0.68**	**1.24**	**0.18**	**−0.01**
	TC	**−0.94**	**−1.00**	**−0.89**	**0.34**	**−0.02**
15	STC	**−1.05**	**−1.22**	**−0.90**	**0.13**	**0.00**
	TC	**−0.55**	**−0.59**	**−0.51**	**0.25**	**−0.01**
16	STC	**0.36**	**0.27**	**0.44**	**0.20**	**−0.01**
	TC	**−0.81**	**−0.89**	**−0.73**	**0.31**	**0.00**
17	STC	**−2.02**	**−2.13**	**−1.92**	**0.12**	**0.00**
	TC	**−1.45**	**−1.48**	**−1.43**	**0.24**	**0.00**
18	STC	**0.34**	**0.14**	**0.52**	**0.20**	**−0.02**
	TC	**−0.31**	**−0.36**	**−0.25**	**0.28**	**−0.04**
19	STC	**0.31**	**0.15**	**0.47**	**0.23**	**−0.03**
	TC	**−0.10**	**−0.17**	**−0.03**	**0.34**	**−0.06**
20	STC	−0.13	−0.24	0.00	0.12	0.00
	TC	**−0.29**	**−0.33**	**−0.25**	**0.53**	**−0.02**
21	STC	0.015	−0.052	0.086	0.18	−0.01
	TC	**−0.12**	**−0.17**	**−0.09**	**0.45**	**−0.04**
22	STC	**0.18**	**0.17**	**0.19**	**0.24**	**−0.01**
	TC	**0.17**	**0.15**	**0.19**	**0.34**	**−0.02**
23	STC	−0.10	−0.26	0.032	0.19	−0.01
	TC	**−0.55**	**−0.63**	**−0.48**	**0.27**	**−0.02**

[a]Results are shown for the model with spatial correlation terms (STC) and without (TC). Entries in bold represent regions where the 95% credible interval does not include 0, i.e., a trend is most likely present. All regions in the model without spatial correlation are likely exhibiting a trend. The regions are as follows: (1) Eastern Tropical Atlantic Province, (2) Indian Monsoon Gyres Province, (3) Indian South Subtropical Gyre Province, (4) North Atlantic Tropical Gyral Province, (5) North Pacific Equatorial Countercurrent Province, (6) North Pacific Tropical Gyre Province, (7) Pacific Equatorial Divergence Province, (8) South Atlantic Gyral Province, (9) West Pacific Warm Pool Province, (10) Western Tropical Atlantic Province, (11) Gulf Stream Province, (12) Kuroshio Current Province, (13) North Atlantic Drift Province, (14) North Atlantic Subtropical Gyral Province (East), (15) North Atlantic Subtropical Gyral Province (West), (16) North Pacific Polar Front Province, (17) North Pacific Subtropical Gyre Province (West), (18) Pacific Subarctic Gyres Province (East), (19) Pacific Subarctic Gyres Province (West), (20) South Pacific Subtropical Gyre Province, (21) South Subtropical Convergence Province, (22) Subantarctic Province, and (23) Tasman Sea Province.

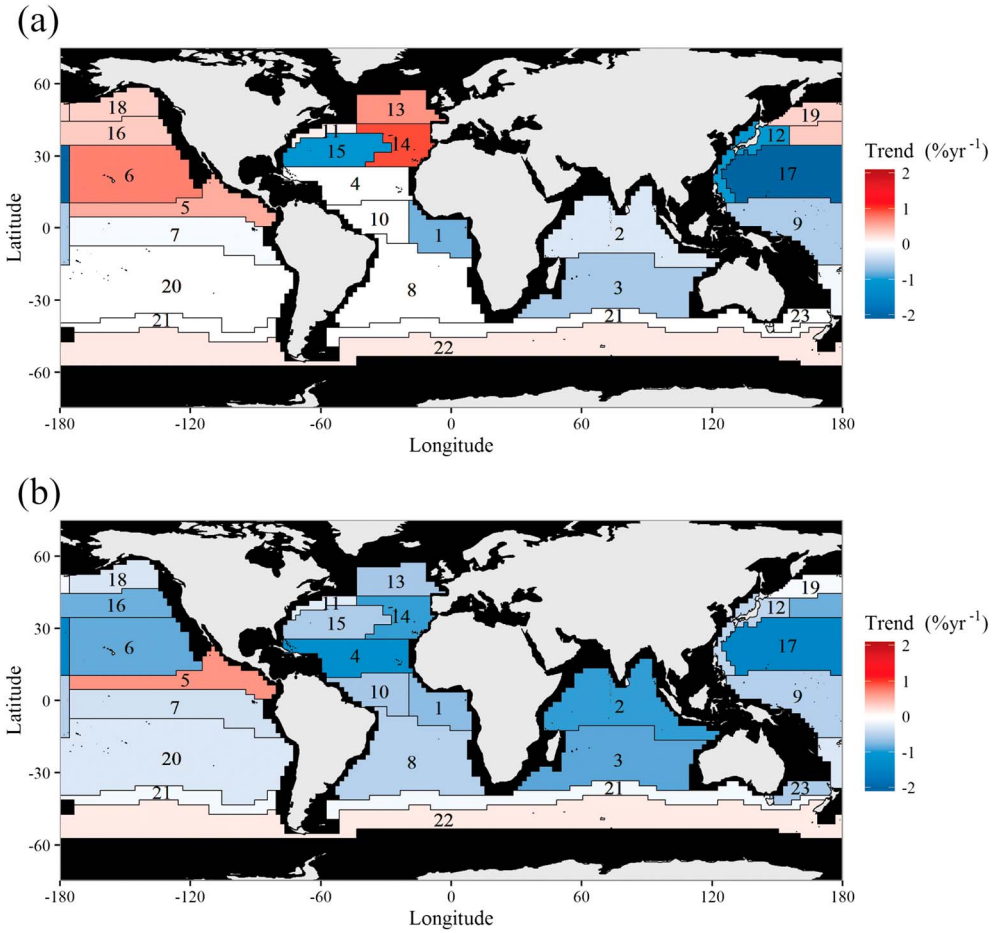

Figure 3. Magnitude of the chl concentration trend detected in each region using ESA OC-CCI data (Sep 1997 to Dec 2013) for (a) the spatiotemporal model and (b) using the model without spatial correlation. Black regions are not considered in the analysis due to limited data availability. Regions that are white indicate that the absence of a trend is most likely based on a 95% credible interval. The regions are as follows: (1) Eastern Tropical Atlantic Province, (2) Indian Monsoon Gyres Province, (3) Indian South Subtropical Gyre Province, (4) North Atlantic Tropical Gyral Province, (5) North Pacific Equatorial Countercurrent Province, (6) North Pacific Tropical Gyre Province, (7) Pacific Equatorial Divergence Province, (8) South Atlantic Gyral Province, (9) West Pacific Warm Pool Province, (10) Western Tropical Atlantic Province, (11) Gulf Stream Province, (12) Kuroshio Current Province, (13) North Atlantic Drift Province, (14) North Atlantic Subtropical Gyral Province (East), (15) North Atlantic Subtropical Gyral Province (West), (16) North Pacific Polar Front Province, (17) North Pacific Subtropical Gyre Province (West), (18) Pacific Subarctic Gyres Province (East), (19) Pacific Subarctic Gyres Province (West), (20) South Pacific Subtropical Gyre Province, (21) South Subtropical Convergence Province, (22) Subantarctic Province, and (23) Tasman Sea Province.

4. Discussion

4.1. Effect of Including Spatial Correlation

Phytoplankton are correlated spatially due to physical and biogeochemical controls, as is expressed in phytoplankton blooms and oligotrophic gyres. By formally including spatial correlation, we model the physical reality of the problem more closely and make the best use of the large amount of spatial data provided by satellite observations, which should help compensate for the relative shortness of the length of record.

A direct comparison of the accuracy between models with and without spatial correlation is shown in Figures 2b and 2c. Including spatial correlation provides an improved fit in all the regions we consider, without exception. In addition, its inclusion leads to more positive values of the trend, in some cases changing the sign. The global average weighted trend is an order of magnitude smaller when including spatial correlation in the model, a result of the presence of both positive and negative trends in the spatial correlation model (compared to almost entirely negative trends in the model without spatial correlation).

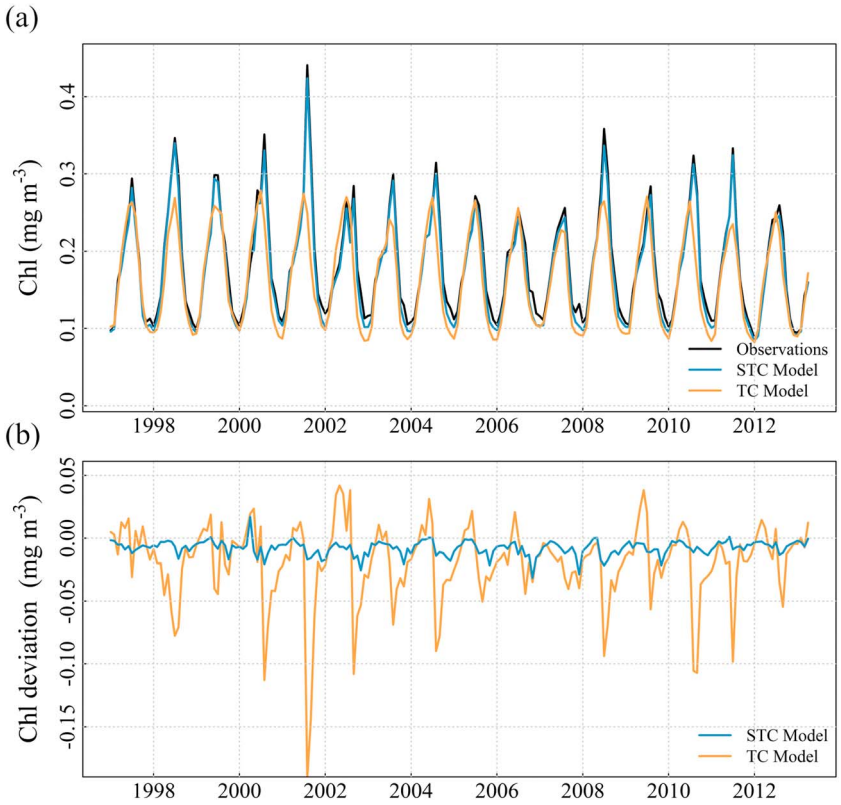

Figure 4. Comparison of observed and modeled chl for the North Atlantic Subtropical Gyral Province (East) (Region 14). (a) Regionally averaged observed and modeled chl time series, and (b) model deviations from observations. Two models are used: STC refers to the model with spatiotemporal correlation and TC refers to the model with temporal correlation only (i.e., without spatial correlation). Note that by considering spatial correlation, the model better captures the full extent of both interannual and seasonal variability.

Despite the poorer fit, the 95% credible intervals for the model without spatial correlation are narrower in all regions except the Subantarctic Province (Region 22). A comparison of the full posterior probability distributions of trends for the two model types in all regions is presented in Figure S3 (supporting information). The Subantarctic Province (Region 22) may present an exception as in both models the uncertainty is very narrow, representing a tightly constrained trend in this region. This regional difference in uncertainty amounts to a global weighted uncertainty 3 times larger in the model with spatial correlation, i.e., the 95% credible interval width is 0.12% yr^{-1} in the model with spatial correlation and 0.045% yr^{-1} in the model without spatial correlation. By ignoring spatial correlation, we treat each site as statistically independent, ignoring the fact that neighboring sites provide similar information. As such, using a model that does not consider spatial correlation will result in an underestimation of the uncertainty due to overuse of the same information.

By comparing average time series for individual regions and the deviations between the observations and model fit (one example in Figure 4, all regions can be found in Figure S2, supporting information) we can examine the cause of the large differences between the two approaches. First, without spatial correlation the model consistently underestimates the observations, which may be in part a result of fitting one model for the whole region, despite annual peak chl concentration occurring at somewhat different times of year throughout the region. By producing a model for the whole region without considering spatial correlation the peaks are essentially smoothed out. However, in some of the largest regions, such as in the South Pacific Subtropical Gyre Province (Region 20), the underestimation occurs equally throughout the year. In these regions, it may be especially important to include additional environmental indicators to explain interannual variability in chl observations when ignoring spatial correlation. The regional variance in these additional environmental factors may make up for the lack of spatial information in the simpler model. Second, and most importantly, without spatial correlation the model seems unable to capture interannual

variability, particularly in months of peak concentration, a very important factor in chlorophyll variability. In both models, there is a tendency to underestimate the observations. This is due to the logarithmic transform, which removes the more extreme high values. The closer fits produced by the spatiotemporal model suggest that it results in more robust trend estimates.

4.2. Effect of Including the Monthly Factor and SST Covariates

To isolate the linear temporal trend from natural variability and the seasonal cycle, we include two additional covariates: SST and a monthly factor. However, SST also exhibits a long-term trend, which is a proxy for the primary proposed driver of changes in chl (i.e., stratification). The seasonality of phytoplankton is also projected to show a long-term trend [*Henson et al*., 2013], which is likely caused by the long-term trend in SST. Thus, the trends we estimate may represent the remaining trends in chl concentration that are not directly related to changing SST. By comparing the model without spatial correlation to other studies, we find that the trend magnitudes and directions detected in most regions of our study are similar (see section below in comparison with other studies). Additionally, the relationship between the SST and trend covariates does not appear to change between model types, i.e., with and without spatial correlation (see supporting information, Figure S4). This suggests that the SST covariate does not contain a significant portion of the chl trend and that the trend terms we estimate can be considered the total trend over the period.

The SST covariate is included to consider some effects of natural variability, which improves fit and allows us to obtain better trend estimates. However, the chl trend detected here is ultimately a response to external forcings and natural variability, which may include SST. This study focuses on trend detection, which aims to verify whether chl has changed in a statistical sense. Formally separating the effects of anthropogenic and natural external forcings would require an attribution study [e.g., *Hegerl et al*., 2010], which is outside the scope of this work.

4.3. Model Fit

The regions with the worst fit to observations (highest NRMSE values) are, in the model with spatial correlation, the North Atlantic Tropical Gyral Province (Region 4) and the Kuroshio Current Province (Region 12). The Kuroshio Current Province (Region 12) includes coastal waters that we typically exclude from this study. Therefore, our trend estimate is likely to suffer from observational issues in coastal regions, which lead to an increased uncertainty in this region. The North Atlantic Tropical Gyre Province (Region 4) could be influenced by Saharan dust either stimulating chl growth or introducing errors into the satellite data [*Kaufman et al*., 2005]. However, this does not seem to affect the Western Tropical Atlantic Province (Region 10) in the same way.

A possible approach to improving the model lies in altering the representation of seasonality. Our model currently uses a fixed seasonality, where there is assumed to be no shift in the phase of the annual cycle of phytoplankton abundance during the 16 year time series, which is at odds with previous studies which observe interannual variability [e.g., *Henson et al*., 2009; *Racault et al*., 2012] and project trends [*Henson et al*., 2013] in bloom phenology. Research has shown that permitting interannual change in seasonality within a model allows for more of the variability to be explained [*Vantrepotte and Mélin*, 2011]. Allowing for interannual change in seasonality is currently incompatible with the model, but it could potentially achieve a closer model fit throughout the time series, particularly in those months and regions where blooms are expected.

Another approach to improving model fit is to consider an anisotropic spatial correlation, which depends on the direction, in addition to the distance, between two sites. Allowing anisotropic spatial correlation could potentially further improve the model accuracy by better representing the effects of ocean currents. However, we stress the large improvement in model fit resulting from the inclusion of isotropic spatial correlation, and any improvements beyond this are expected to be minimal.

4.4. Region Selection

The data are divided into Longhurst provinces, which are defined by their characteristic biogeochemical and physical forcings, and thus, each province should exhibit an approximately uniform trend within its borders. The region boundaries as defined in *Henson et al*. [2010] are explored as an alternative in the supporting information (Text S4). Dividing the data by Longhurst provinces leads to smaller region sizes than some other divisions, e.g., *Henson et al*. [2010], which leads to faster computation time and allows a more detailed regional

picture to be revealed. Any division introduces a degree of "edge effect," as grid cells located at the edges of the region do not consider the full range of points within their spatial correlation range. However, including information from grid cells outside a Longhurst region may result in poor estimates as the trends and behaviors there are expected to be different.

As physical and biogeochemical conditions change into the future, the location of boundaries separating different provinces is also expected to change. For example, it has already been noted that oligotrophic gyre regions may be expanding, reportedly in the range of 0.8–4.3% yr^{-1} [*Irwin and Oliver*, 2009; *Polovina et al*., 2008]. Recent work has considered region boundaries that are dynamic in time [e.g., *Reygondeau et al*., 2013]. The use of predefined regions in the present study ignores the effect of potential change in region boundaries, which could affect the trend estimates. Thus, temporal changes in a dynamic region boundary would lead to a portion of the static region belonging to a different biogeochemical region with a different trend. Some ocean regions have been reported to be changing in the range of 0.8–4.3% yr^{-1} [*Polovina et al*., 2008], though a proportion of this is likely interannual variability. Thus, a relatively small change in region boundaries over the period of the ESA OC-CCI data set may be present. A modest improvement in model fit accuracy is expected from implementing dynamic boundaries, but this should be the focus of future work.

4.5. Choice of Priors

One of the strengths of Bayesian analysis is the use of "priors" that represent, in the model framework, previous understanding of the particular topic. For this study, priors could have been formulated using independent information from previous studies on the relationship of chl with SST or the magnitudes, and directions, of chl trends. Instead, flat priors are used, i.e., the prior distributions have large variance reflecting a lack of knowledge about the chl trends and other parameters estimated in the model. As the focus of this work is to assess the effect of including spatial correlation when estimating chl trends, providing prior information may inhibit a complete comparison. In future work the authors intend to use prior information for a more complete understanding of global trends.

4.6. Comparison With Previous Studies

For a number of regions, the trends estimated using the spatiotemporal model are of a similar magnitude to other studies, particularly to satellite studies carried out on a more regional scale [e.g., *Vantrepotte and Mélin*, 2011; *Saulquin et al*., 2013; *Siegel et al*., 2013]. However, there are a few regions where we estimate trends of the opposite magnitude, particularly in the North Pacific and North Atlantic. These differences can be attributed to both the different approach and a longer time span used compared to previous studies. There are a limited number of studies considering a time span as long as considered here; these include *Gregg and Rousseaux* [2014] and *Signorini et al*. [2015], although neither uses the Longhurst region divisions. Both studies agree more closely with the trends estimated using the model without spatial correlation rather than the model with spatial correlation. This is because both *Gregg and Rousseaux* [2014] and *Signorini et al*. [2015] use regional average time series, an approach more consistent with the model without spatial correlation presented here. When comparing the results of these two studies to the trends obtained from the model with spatial correlation, there is an agreement in the Equatorial Atlantic, the South Atlantic, the South Pacific, much of the Indian Ocean, and the Southern Ocean. The most significant differences are in the subpolar North Atlantic and North Pacific, where our study shows positive trends.

More specifically, the North Pacific shows the biggest difference from *Gregg and Rousseaux* [2014] and *Signorini et al*. [2015] where we find positive trends over the eastern and northern extents. This is most likely a result of the strong influence of the El Niño–Southern Oscillation (ENSO) on chl in the region and the improved fit to interannual variability provided by the inclusion of spatial correlation in the model. It should be noted that the North Pacific Equatorial Countercurrent Province (Region 5) is strongly positive in both the models we calculate, contrary to the trends estimated by *Gregg and Rousseaux* [2014]. The difference is likely due to the different timescales and the different approaches used to account for seasonal variability, as *Gregg and Rousseaux* [2014] model trends in annual medians of monthly means. In addition, including SST within the model helps to explain the interannual variability, as ENSO is associated with large SST variation in the Pacific.

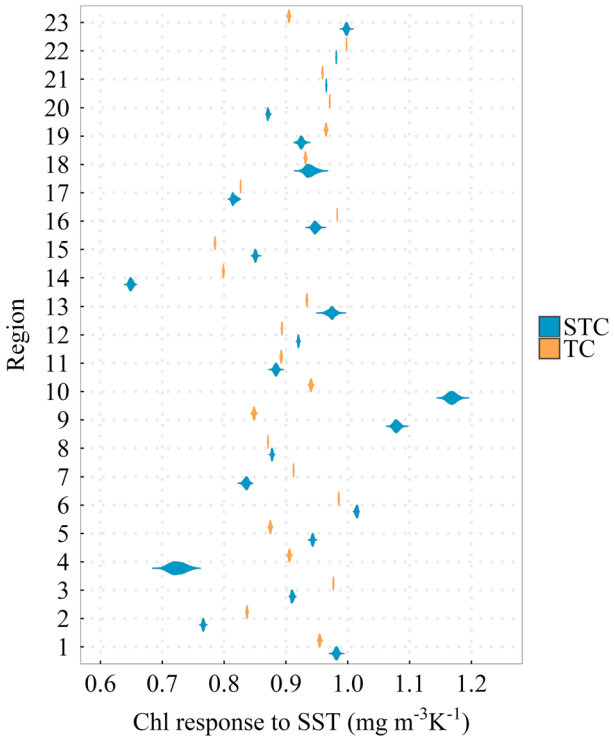

Figure 5. Posterior probability densities for the response of chl to SST (i.e., the SST covariate) in each region. Two models are used in each region: STC refers to the model with spatiotemporal correlation and TC refers to the model with temporal correlation only (i.e., without spatial correlation terms). The regions are as follows: (1) Eastern Tropical Atlantic Province, (2) Indian Monsoon Gyres Province, (3) Indian South Subtropical Gyre Province, (4) North Atlantic Tropical Gyral Province, (5) North Pacific Equatorial Countercurrent Province, (6) North Pacific Tropical Gyre Province, (7) Pacific Equatorial Divergence Province, (8) South Atlantic Gyral Province, (9) West Pacific Warm Pool Province, (10) Western Tropical Atlantic Province, (11) Gulf Stream Province, (12) Kuroshio Current Province, (13) North Atlantic Drift Province, (14) North Atlantic Subtropical Gyral Province (East), (15) North Atlantic Subtropical Gyral Province (West), (16) North Pacific Polar Front Province, (17) North Pacific Subtropical Gyre Province (West), (18) Pacific Subarctic Gyres Province (East), (19) Pacific Subarctic Gyres Province (West), (20) South Pacific Subtropical Gyre Province, (21) South Subtropical Convergence Province, (22) Subantarctic Province, and (23) Tasman Sea Province. Note the significantly smaller uncertainty by comparison with Figure 2.

High-latitude regions also consistently show positive trends in our study, which has not been observed in other satellite studies [e.g., *Gregg and Rousseaux*, 2014; *Vantrepotte and Mélin*, 2011]. However, this result is consistent with other longer-term observational studies such as *Martinez et al.* [2016], which showed an increase in phytoplankton abundance since the 1960s in North Atlantic Continuous Plankton Recorder data. The similarity to results from a longer-term study could indicate our method's improved ability to isolate a secular trend from seasonal and interannual variability. This result also follows the theoretical framework where phytoplankton abundance is affected by increasing SST, leading to decreased phytoplankton abundance in nutrient limited regions and increased phytoplankton abundance in light limited areas [*Doney*, 2006]. However, contrary to expectations for nutrient limited regions, the SST covariate values determined by the model are positive, indicating chl is increasing with SST, in all regions (see Figure 5). This may suggest that in our model the monthly factor accounts for the majority of the variability, particularly seasonal, expected to be associated with SST.

Model projections show an overall global decrease in chl, associated with a global SST increase and associated increases in grazing except in major sea ice-forming regions, the subpolar North Pacific, and the South Pacific [*Bopp et al.*, 2013; *Cabré et al.*, 2015; *Laufkötter et al.*, 2015]. Hindcast models (covering 1960–2006) show similar results but with a more mixed pattern in the Southern Ocean and increases in the subpolar North Atlantic [*Laufkötter et al.*, 2013].

The regional patterns of decline detected in our study do not correspond to the pattern of trends detected in a longer-term compilation of multiple observational sources by *Boyce et al.* [2014]. This disparity would suggest that, despite the increased robustness of the trends detected using a spatiotemporal model, in a number of regions the shortness of the record still challenges the detection of a long-term trend. Alternatively, this disparity may arise from using a multisensor data set, i.e., one that contains data from multiple satellite sensors. Due to only a partial temporal overlap and bias between individual sensors, there is the potential for multisensor data sets to introduce discontinuities in the record. Such discontinuities have been shown to potentially impact trends estimated in a multisensor data sets, due to uncorrected biases, potentially leading to misleading conclusions [*Mélin*, 2016]. The ESA OC-CCI data set used here has undergone an extensive

bias-correction process, so it will be affected by this issue to a more limited degree. Assessing the presence and effect of discontinuities in multisensor records in this model framework is the focus of ongoing work.

5. Conclusions

This study presents, to our knowledge, the first Bayesian spatiotemporal analysis of trends in ocean chlorophyll. The Bayesian spatiotemporal analysis (1) provides a more accurate fit to observations, (2) provides a more complete assessment of uncertainty, and (3) impacts trend estimates when compared to a model that is not spatially resolved. For example, the global trend in chl from our spatiotemporal model is an order of magnitude smaller ($-0.023 \pm 0.12\%\ yr^{-1}$), than the trend detected ($-0.38 \pm 0.045\%\ yr^{-1}$) using a model without spatial correlation, and has an approximately 3 times larger uncertainty. This result suggests that trend analysis using statistical models that are not spatially resolved might lead to biased and overconfident trend estimates. The significant differences between the two approaches (i.e., with and without spatial correlation) suggest it is important to fully consider space-time effects when assessing the impacts of climate change, particularly for data sets with large uncertainty or with a short record length. Another innovative aspect of this study is the use of a Bayesian approach that provides the advantage of quantifying the full probability distribution of trends in each region.

While the detected global decline in chl over the period September 1997 to December 2013 is small, there is a regional disparity with both positive and negative trends present across the globe ranging from approximately $-2\%\ yr^{-1}$ to $1\%\ yr^{-1}$. If sustained, these changes could result in a cascade effect throughout the entire trophic system via trophic amplification by changing the available food supply. Changes in phytoplankton abundance also impact the carbon cycle with potential feedbacks throughout the biogeochemical system. We detect increasing concentration in high-latitude regions, which are dominated by large phytoplankton species. This result could suggest an increasing carbon export to the deep ocean in these regions, a potential climate feedback, although we do not assess changes in specific species.

By including environmental covariates to explain seasonal and interannual variability we can more clearly distinguish the secular trend within the available data. However, with only 16 years of data it may still not be possible to distinguish a long-term response to climate change from natural variability in all regions, especially where the signal-to-noise ratio is small. Future work should aim to include additional data sets (e.g., in situ data) for additional information and to increase the period covered in the analysis. Combining evidence from different and independent data sets offers the potential to increase confidence in the trends detected and to determine whether they can be distinguished from interannual variability, which can be achieved within the space-time modeling framework. We stress the solution offered by space-time modeling for quantifying global change in general.

Acknowledgments
The authors are grateful to the ESA for providing the OC-CCI ocean color data set used here as well as the NOAA for providing the Optimum Interpolation SST data set. The data can be found at the following respective URLs http://www.esa-oceancolour-cci.org/ and http://www.esrl.noaa.gov/psd/data/gridded/data.noaa.oisst.v2.html. The code is made publicly available at https://github.com/oceanstats/Chlorophyll-trends. M.L.H. was partially funded by the University of Southampton Vice Chancellor's Studentship Award. C.B. was supported by a Marie Curie FP7 Reintegration Grants within the Seventh European Community Framework (project 631466 - TROPHYZ).

References

Antoine, D., A. Morel, H. R. Gordon, V. F. Banzon, and R. H. Evans (2005), Bridging ocean color observations of the 1980s and 2000s in search of long-term trends, *J. Geophys. Res.*, *110*, C06009, doi:10.1029/2004JC002620.

Bakar, K. S., and S. K. Sahu (2015), Sp timer: Spatio-temporal Bayesian modeling using R, *J. Stat. Softw.*, *63*(15), 1–32.

Banerjee, S., A. E. Gelfand, A. O. Finley, and H. Sang (2008), Gaussian predictive process models for large spatial data sets, *J. R. Stat. Soc. Ser. B*, *70*, 825–848.

Beaulieu, C., S. A. Henson, J. L. Sarmiento, J. P. Dunne, S. C. Doney, R. R. Rykaczewski, and L. Bopp (2013), Factors challenging our ability to detect long-term trends in ocean chlorophyll, *Biogeosciences*, *10*(4), 2711–2724, doi:10.5194/bg-10-2711-2013.

Behrenfeld, M. J., R. T. O'Malley, D. A. Siegel, C. R. McClain, J. L. Sarmiento, G. C. Feldman, A. J. Milligan, P. G. Falkowski, R. M. Letelier, and E. S. Boss (2006), Climate-driven trends in contemporary ocean productivity, *Nature*, *444*(7120), 752–755. [Available at http://www.nature.com/nature/journal/v444/n7120/suppinfo/nature05317_S1.html].

Bélanger, S., M. Babin, and J. Tremblay (2013), Increasing cloudiness in Arctic damps the increase in phytoplankton primary production due to sea ice receding, *Biogeosciences*, *10*(6), 4087–4101.

Bopp, L., et al. (2013), Multiple stressors of ocean ecosystems in the 21st century: Projections with CMIP5 models, *Biogeosciences*, *10*(10), 6225–6245, doi:10.5194/bg-10-6225-2013.

Boyce, D. G., M. R. Lewis, and B. Worm (2010), Global phytoplankton decline over the past century, *Nature*, *466*(7306), 591–596, doi: 10.1038/Nature09268.

Boyce, D. G., M. Dowd, M. R. Lewis, and B. Worm (2014), Estimating global chlorophyll changes over the past century, *Prog. Oceanogr.*, *122*, 163–173, doi:10.1016/j.pocean.2014.01.004.

Cabré, A., I. Marinov, and S. Leung (2015), Consistent global responses of marine ecosystems to future climate change across the IPCC AR5 Earth system models, *Clim. Dyn.*, *45*(5–6), 1253–1280.

Campbell, J. W. (1995), The lognormal distribution as a model for bio-optical variability in the sea, *J. Geophys. Res.*, *100*(C7), 13237–13254, doi: 10.1029/95JC00458.

Chandler, R. E., and E. M. Scott (2011), Other issues, in *Statistical Methods for Trend Detection and Analysis in the Environmental Sciences, Edited*, pp. 235–236, John Wiley, Chichester, England.

Collins, M., et al. (2013), Long-term climate change: Projections, commitments and irreversibility, in *Climate Change 2013: The Physical Science Basis. Contribution of Working Group I to the Fifth Assessment Report of the Intergovernmental Panel on Climate Change*, edited by T. F. Stocker et al., pp. 1029–1136, Cambridge Univ. Press, Cambridge, U. K., and New York.

Doney, S. C. (2006), Oceanography—Plankton in a warmer world, *Nature*, *444*(7120), 695–696, doi:10.1038/444695a.

England, M. H., S. McGregor, P. Spence, G. A. Meehl, A. Timmermann, W. Cai, A. S. Gupta, M. J. McPhaden, A. Purich, and A. Santoso (2014), Recent intensification of wind-driven circulation in the Pacific and the ongoing warming hiatus, *Nat. Clim. Change*, *4*(3), 222–227, doi:10.1038/nclimate2106.

Field, C. B., M. J. Behrenfeld, J. T. Randerson, and P. Falkowski (1998), Primary production of the biosphere: Integrating terrestrial and oceanic components, *Science*, *281*(5374), 237–240, doi:10.1126/science.281.5374.237.

Finley, A. O., H. Y. Sang, S. Banerjee, and A. E. Gelfand (2009), Improving the performance of predictive process modeling for large datasets, *Comput. Stat. Data Anal.*, *53*(8), 2873–2884, doi:10.1016/j.csda.2008.09.008.

Gregg, W. W., and C. S. Rousseaux (2014), Decadal trends in global pelagic ocean chlorophyll: A new assessment integrating multiple satellites, in situ data, and models, *J. Geophys. Res. Oceans*, *119*, 5921–5933, doi:10.1002/2014JC010158.

Handcock, M. S., and M. L. Stein (1993), A Bayesian-analysis of kriging, *Technometrics*, *35*(4), 403–410, doi:10.2307/1270273.

Handcock, M. S., and J. R. Wallis (1994), An approach to statistical spatial-temporal modeling of meteorological fields, *J. Am. Stat. Assoc.*, *89*(426), 368–378, doi:10.2307/2290832.

Hegerl, G. C., O. Hoegh-Guldberg, G. Casassa, M. P. Hoerling, R. S. Kovats, C. Parmesan, D. W. Pierce, and P. A. Stott (2010), Good practice guidance paper on detection and attribution related to anthropogenic climate change, in *Meeting Report of the Intergovernmental Panel on Climate Change Expert Meeting on Detection and Attribution of Anthropogenic Climate Change*, edited by T. F. Stocker et al., pp. 2–8, IPCC Working Group I Tech. Support Unit, Univ. of Bern, Bern, Switzerland.

Henson, S., H. Cole, C. Beaulieu, and A. Yool (2013), The impact of global warming on seasonality of ocean primary production, *Biogeosciences*, *10*(6), 4357–4369, doi: 10.5194/bg-10-4357-2013.

Henson, S. A., J. P. Dunne, and J. L. Sarmiento (2009), Decadal variability in North Atlantic phytoplankton blooms, *J. Geophys. Res.*, *114*, C04013, doi:10.1029/2008JC005139.

Henson, S. A., J. L. Sarmiento, J. P. Dunne, L. Bopp, I. Lima, S. C. Doney, J. John, and C. Beaulieu (2010), Detection of anthropogenic climate change in satellite records of ocean chlorophyll and productivity, *Biogeosciences*, *7*(2), 621–640.

Hoegh-Guldberg, O., R. Cai, E. S. Poloczanska, P. G. Brewer, S. Sundby, K. Hilmi, V. J. Fabry, and S. Jung (2014), The ocean, in climate change 2014: Impacts, adaptation, and vulnerability. Part B: Regional aspects, in *Contribution of Working Group II to the Fifth Assessment Report of the Intergovernmental Panel of Climate Change*, edited by V. R. Barros et al., pp. 1655–1731, Cambridge Univ. Press, Cambridge, U. K., and New York.

Hyde, K. J. W., J. E. O'Reilly, and C. A. Oviatt (2007), Validation of SeaWiFS chlorophyll a in Massachusetts Bay, *Cont. Shelf Res.*, *27*(12), 1677–1691, doi:10.1016/j.csr.2007.02.002.

Irwin, A. J., and M. J. Oliver (2009), Are ocean deserts getting larger?, *Geophys. Res. Lett.*, *36*, L18609, doi:10.1029/2009GL039883.

Kaufman, Y., I. Koren, L. Remer, D. Tanré, P. Ginoux, and S. Fan (2005), Dust transport and deposition observed from the Terra-Moderate Resolution Imaging Spectroradiometer (MODIS) spacecraft over the Atlantic Ocean, *J. Geophys. Res.*, *110*, D10S12, doi:10.1029/2003JD004436.

Kirtman, B., et al. (2013), Near-term climate change: Projections and predictability, in *Climate Change 2013: The Physical Science Basis. Contribution of Working Group I to the Fifth Assessment Report of the Intergovernmental Panel on Climate Change*, edited by T. F. Stocker et al., pp. 993–994, Cambridge Univ. Press, Cambridge, U. K., and New York.

Kruschke, J. R. (2015), *Doing Bayesian Data Analysis*, 2nd ed., pp. 15–32, A Tutorial with R, JAGS, and Stan. Academic Press/Elsevier, Boston, Mass, isbn:9780124058880.

Laufkötter, C., M. Vogt, and N. Gruber (2013), Long-term trends in ocean plankton production and particle export between 1960–2006, *Biogeosciences*, *10*(11), 7373–7393.

Laufkötter, C., M. Vogt, N. Gruber, M. Aita-Noguchi, O. Aumont, L. Bopp, E. Buitenhuis, S. Doney, J. Dunne, and T. Hashioka (2015), Drivers and uncertainties of future global marine primary production in marine ecosystem models, *Biogeosciences*, *12*, 6955–6984.

Lavender, S., T. Jackson, and S. Sathyendranath (2015), The ocean colour climate change initiative, *Ocean Challenge*, *21*(1), 3.

Longhurst, A. (1995), Seasonal cycles of pelagic production and consumption, *Prog. Oceanogr.*, *36*(2), 77–167, doi:10.1016/0079-6611(95)00015-1.

Longhurst, A. (1998), *Ecological Geography of the Sea*, pp. 103–114, Academic Press, San Diego, Calif.

Martinez, E., D. E. Raitsos, and D. Antoine (2016), Warmer, deeper, and greener mixed layers in the North Atlantic subpolar gyre over the last 50 years, *Global Change Biol.*, *22*(2), 604–612, doi:10.1111/gcb.13100.

Mélin, F. (2016), Impact of inter-mission differences and drifts on chlorophyll-*a* trend estimates, *Int. J. Remote Sens.*, *37*(10), 2233–2251, doi:10.1080/01431161.2016.1168949.

Mélin, F., G. Zibordi, and J.-F. Berthon (2007), Assessment of satellite ocean color products at a coastal site, *Remote Sens. Environ.*, *110*(2), 192–215.

Moore, G., K. Våge, R. Pickart, and I. Renfrew (2015), Decreasing intensity of open-ocean convection in the Greenland and Iceland seas, *Nat. Clim. Change*, *5*, 877–882.

Polovina, J. J., E. A. Howell, and M. Abecassis (2008), Ocean's least productive waters are expanding, *Geophys. Res. Lett.*, *35*, L03618, doi:10.1029/2007GL031745.

Racault, M. F., C. Le Quere, E. Buitenhuis, S. Sathyendranath, and T. Platt (2012), Phytoplankton phenology in the global ocean, *Ecol. Indic.*, *14*(1), 152–163, doi:10.1016/j.ecolind.2011.07.010.

Rayner, N. A., D. E. Parker, E. B. Horton, C. K. Folland, L. V. Alexander, D. P. Rowell, E. C. Kent, and A. Kaplan (2003), Global analyses of sea surface temperature, sea ice, and night marine air temperature since the late nineteenth century, *J. Geophys. Res.*, *108*(D14), 4407, doi: 10.1029/2002jd002670.

Reygondeau, G., A. Longhurst, E. Martinez, G. Beaugrand, D. Antoine, and O. Maury (2013), Dynamic biogeochemical provinces in the global ocean, *Global Biogeochem. Cycles*, *27*, 1046–1058, doi:10.1002/gbc.20089.

Reynolds, R. W., N. A. Rayner, T. M. Smith, D. C. Stokes, and W. Q. Wang (2002), An improved in situ and satellite SST analysis for climate, *J. Clim.*, *15*(13), 1609–1625, doi:10.1175/1520-0442(2002)015<1609:Aiisas>2.0.Co;2.

Rykaczewski, R. R., and J. P. Dunne (2011), A measured look at ocean chlorophyll trends, *Nature*, *472*(7342), E5-E6, doi:10.1038/Nature09952.

Sahu, S. K., and K. S. Bakar (2012), Hierarchical Bayesian autoregressive models for large space-time data with applications to ozone concentration modelling, *Appl. Stoch. Model. Bus.*, *28*(5), 395–415, doi:10.1002/asmb.1951.

Saulquin, B., R. Fablet, A. Mangin, G. Mercier, D. Antoine, and O. Fanton d'Andon (2013), Detection of linear trends in multisensor time series in the presence of autocorrelated noise: Application to the chlorophyll-a SeaWiFS and MERIS data sets and extrapolation to the incoming sentinel 3-OLCI mission, *J. Geophys. Res. Oceans*, *118*, 3752–3763, doi:10.1002/jgrc.20264.

Schollaert, S. E., J. A. Yoder, J. E. O'Reilly, and D. L. Westphal (2003), Influence of dust and sulfate aerosols on ocean color spectra and chlorophyll a concentrations derived from SeaWiFS off the U. S. east coast, *J. Geophys. Res.*, *108*(C6), 3191, doi:10.1029/2000JC000555.

Siegel, D. A., et al. (2013), Regional to global assessments of phytoplankton dynamics from the SeaWiFS mission, *Remote Sens. Environ.*, *135*, 77–91, doi:10.1016/j.rse.2013.03.025.

Signorini, S. R., B. A. Franz, and C. R. McClain (2015), Chlorophyll variability in the oligotrophic gyres: Mechanisms, seasonality and trends, *Front. Mar. Sci.*, *2*(1), 1–11, doi: 10.3389/fmars.2015.00001.

Vantrepotte, V., and F. Mélin (2011), Inter-annual variations in the SeaWiFS global chlorophyll *a* concentration (1997–2007), *Deep Sea Res., Part I*, *58*(4), 429–441.